Towards A Generic *In Vivo In Situ* Camera Lens Cleaning Module for Laparoscopic Surgery

Xiaolong Liu* *Member, IEEE,* Hui Liu, Jindong Tan *Member, IEEE*

Abstract— This paper proposes a generic cleaning module to address lens fogging and soiling problems for insertable robotic cameras in laparoscopic surgery. The proposed lens cleaning module features minimal intraoperative interruption for surgeons to maintain clear visual field. The technical challenges for developing such a compact modular design involve confining the wiping mechanism within small space, yet delivering sufficient energy for the lens cleaning task. Inspired by thermo-activated phase transformation of shape memory alloy, we develop an effective mesoscale actuation mechanism to overcome the design challenges. A prototype is designed and manufactured for performance evaluation. The design effectiveness was verified by experiments.

I. INTRODUCTION

Since the emergence of minimally invasive surgery (MIS) in the last century, laparoscopic cameras have been indispensable components for visually guiding surgical instruments in the abdominal cavity [1]. Commercial long-stick laparoscopic cameras (or laparoscopes) integrated with a relay lens imaging channel, external high definition CCD/CMOS cameras, and fiber-optic scope for lighting are currently the gold standard. However, surgeons clinically experience disadvantages by using this type of equipment, including: loss of triangulation, limited field of view, counter intuitive manipulation, and requiring extra dedicated incision [2]. Research efforts have been made to address these inconvenience by developing fully insertable robotic cameras. Technical solutions are proposed to overcome the limitations of a laparoscope, such as magnetic actuation [3], [4], *in vivo* wireless imaging data transmission [5], and optimized *in vivo* illumination [6], [7]. But for an insertable robotic camera, the imaging lens contamination by fogging and/or soiling is a remaining issue which impairs clear visual field during laparoscopic surgery [8].

The fogging problem results from condensation of water vapor due to temperature difference between the abdominal cavity and the operating room [9], while the soiling problem is mainly caused by splashed body fluid and bone dust [8], etc. For conventional laparoscopes, the most common solution is to withdraw the laparoscope and wipe the lens externally. According to clinical investigations, more than 37% of laparoscopy surgery time is done with impaired image [10] due to contamination of a camera lens. Surgeons at least spend 3% extra time for cleaning the contaminated

lens during laparoscopic surgery [11]. These situations increase the procedure length and surgery cost. More seriously, the distraction may affect surgeons' judgment, and may potentially cause patient injury [12]. To solve the fogging and/or soiling problems, alternative methods are proposed such as equipment modifications to a laparoscope, applying anti-fogging chemical coatings, pre-warming of the lens, and inserted cleaning site inside the abdominal cavity [13].

Nevertheless, the existing solutions for laparoscopes are not ideal for the insertable robotic camera designs. It is impractical to retrieve an inserted robotic camera from the abdominal cavity for cleaning the contaminated lens during surgical operation. Anti-fogging coating may alleviate water vapor condensation on the lens, but the transparency of lens may be affected [14]. Moreover, neither anti-fogging coatings nor pre-warming treatments can prevent soiling of a camera lens. To avoid external lens wiping procedure, wiping stations such as an expendable device [15] and wiping sleeves [16] can be inserted through another incision in the abdominal cavity. But an *in vivo* wiping station itself is very likely to get contaminated due to splashed blood and body fluid. Mechanical modification of a laparoscope's cannula is an alternate method for on-site lens cleaning by adding a swab/wiper at the cannula's distal end [17] or a custom fluid/gas injection mechanism [18]. To interact with the distal end swab/wiper on the cannula, axial reciprocating stroke of the laparoscope is required. If similar mechanical designs apply to an insertable camera, it demands peripheral actuation mechanisms that undesirably occupy the very limited on-board space. In addition, the motion of axial stroke wiping can interrupt an on-going surgical procedure due to change of the camera's field of view.

The scope of this paper is to provide a lens cleaning method with minimal intraoperative interruption for an insertable robotic camera. The minimal intraoperative interruption in this context implies that the lens cleaning procedure shouldn't induce any movement of the camera, and should be completed within seconds. Initial trials towards this goal were carried out by our research group [19]. But, the proposed solutions are design-dependent, and involve DC motors and worm/gear mechanisms for actuating the wipers. There is a need of having a more generic solution that preferably features compact modularized design with integrated actuation and wiping function.

The primary challenge to achieve this objective is the invention of a wiping mechanism that can be confined within very small space, yet can efficiently deliver sufficient energy for the lens cleaning task. Inspired by the ability of shape

∗ Corresponding author: Xiaolong Liu, xliu57@vols.utk.edu
Xiaolong Liu, Hui Liu, and Jindong Tan are with Department of Mechanical, Aerospace and Biomedical Engineering, University of Tennessee, Knoxville, TN 37996 USA
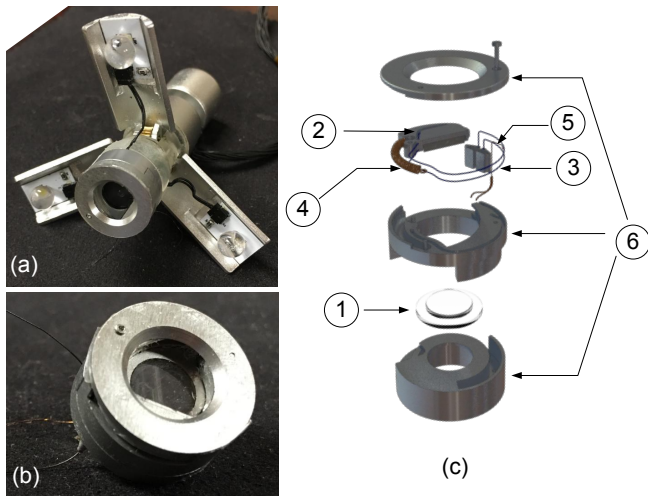
Fig. 1. Prototype illustration of the proposed lens cleaning module. (a) Integrating the lens cleaning module with our transformable robotic camera [6]. (b) Module prototype. (c) Illustration of the module components. ①– optical glass cover; ②– wiping blade; ③–SMA wire; ④–micro spring; ⑤–micro thermistor; ⑥–aluminum structure.

memory alloy (SMA) which memorizes its original shape at low temperature and can recover the deformation with heavy loadings by thermal activation, we propose a generic lens cleaning module based on SMA actuation, as illustrated in Fig. 1(b). The wiping blade is actuated by a current heated SMA wire that conceals at the edge of the module's anodized aluminum alloy structure. Benefiting from this structure, the deactivated SMA wire's temperature rapidly reduces, and subsequently a bias micro spring can reset the wiping blade by elongating the SMA wire that has transformed to the phase of detwinned martensite. This simple and effective lens cleaning module can not only work on our insertable robotic camera that published in [6] (Fig. 1(a)), but it could also be integrated in other surgical robots such as da Vinci SP® and Titan Medical's SPORT surgical system with minor modifications.

II. DESIGN CONCEPT AND WORKING PRINCIPLE

The generic lens cleaning module consists of six major components as shown in Fig. 1(c), which include 1) an optical glass cover (Fig. 1(c)-①) for sealing the imaging sensor, lens and peripheral electronics in a waterproof chamber; 2) a miniature wiping blade (Fig. 1(c)-②) sitting against the optical glass cover; 3) an SMA wire (Fig. 1(c)-③) for actuating the wiping blade; 4) a micro spring (Fig. 1(c)-④) for reseting the wiping blade outside the visual field; 5) a micro thermistor (Fig. 1(c)-⑤) for providing thermo feedback from the SMA; and 6) an anodized aluminum alloy structure (Fig. 1(c)-⑥) that features electrical insulation for the SMA wire and great thermal conductivity for fast heat dissipation. Depending on dimensional requirements, the proposed design can be scaled to an appropriate size for coupling with of a specific *in vivo* robotic camera system.

The working principle of the lens cleaning module involves controlling the SMA wire's material phase by switching the input current. The SMA has two distinct phases,
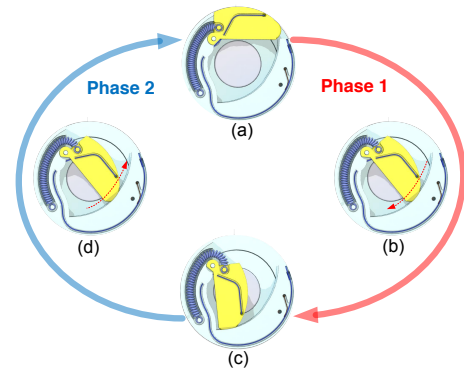

Fig. 2. Actuation cycle of the lens cleaning module. Phase 1: (a)-(b)-(c). Phase 2: (c)-(d)-(a).

i.e., the high temperature phase (austenite) and the low temperature phase (martensite). When a deformed SMA is heated above A_f (austenite finish temperature), the material contracts to recover its original shape by the activated internal driving energy which is capable of overcoming big loading weight [20]. When the SMA is cooled from A_f to M_f (martensite finish temperature) under the condition of zero-load, the material transforms to twinned martensite with unnoticeable macroscale shape change. By providing small loading weight, the SMA transforms from twinned martensite phase to detwinned martensite phase which induces the material's elongation.

Fig. 2 demonstrates actuation process of the lens cleaning module. In idle mode, the wiping blade rests by the side of the optical glass cover as illustrated in Fig. 2(a). The SMA wire is initially set at its elongated shape which is in at the phase of detwinned martensite. A full wiping cycle consists of two consecutive phases: phase 1 (Fig. 2(a)-(b)-(c)) and phase 2 (Fig. 2(c)-(d)-(a)). In phase 1, the SMA wire is activated by Joule heating for transforming to austenite. The resulted contractive deformation shortens the wire length, and consequently the wiping blade is driven to wipe across the optical glass cover. In phase 2, after the wiping blade reaches the state shown in Fig. 2(c), the SMA wire is deactivated by switching off the input current. During cooling process, the stretched micro spring provides bias force to elongate the SMA wire and drive the wiping blade back to the initial state (Fig. 2(a)).

The major issue of developing a functional lens cleaning module is the compatibility between the SMA wire and the micro spring. A stiff micro spring may apply excessive bias force to block the SMA wire for actuating the wiping blade to reach the state in Fig. 2(c), while a soft micro spring may provide insufficient bias force to reset the wiping blade. In the following section, detailed design principle of the lens cleaning module is presented.

III. DESIGN OF ACTUATION MECHANISM

Fig. 3 illustrates actuation analysis of the lens cleaning module. To activate the wiping blade, the torque from the SMA wire τ_w around the rotation axis z has to overcome the torques from the micro spring τ_s and the frictional resistance τ_f during phase 1. In phase 2, τ_s overcomes τ_w and τ_f to
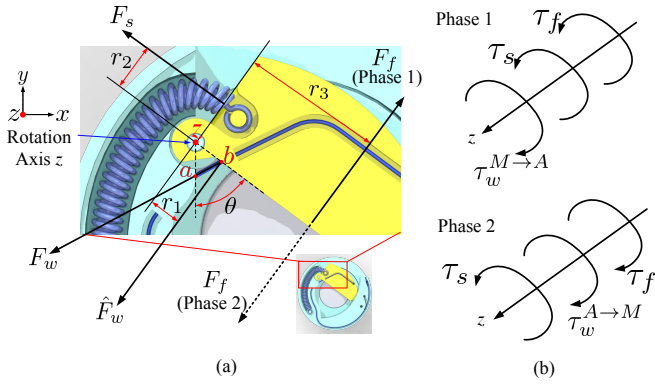
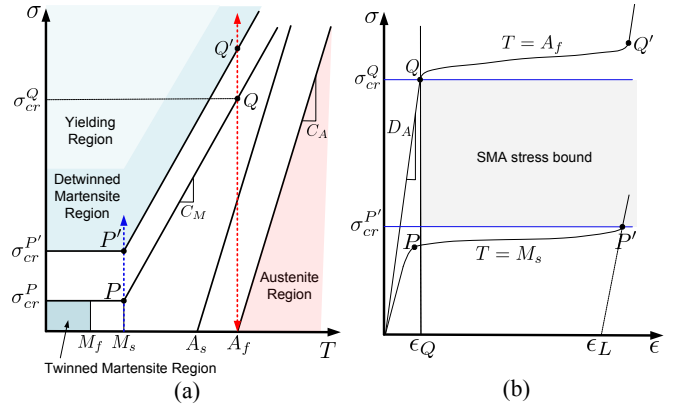Fig. 3. Illustration of actuation mechanism analysis.

Fig. 4. Analysis of SMA properties for the system design. (a) Illustration of SMA phase transformation by stress-temperature relation based on the Brinson's model. The red double-arrow line indicates the SMA's phase transformation by applying different stresses under a constant temperature $T = A_f$ (superelastic behavior). The blue arrow line shows the phase transformation from austenite to detwinned martensite under a constant temperature $T = M_s$. (b) Illustration of SMA stress bound for micro spring design by stress-strain relation.

reset the wiping blade to the initial resting position. This relationship can be represented in (1) and (2), and illustrated in Fig. 3(b).

$$\tau_w^{M \to A} > \tau_s + \tau_f, \tag{1}$$

$$\tau_s > \tau_w^{A \to M} + \tau_f, \tag{2}$$

where $\tau_w^{M \to A}$ and $\tau_w^{A \to M}$ denote SMA wire torque during the phase transformations of martensite-to-austenite and austenite-to-martensite; τ_f represents the frictional torque that is mainly from the contact of the wiping blade and the lens cover.

The strategy of developing an effective actuation mechanism is to firstly determine an SMA wire with specific material properties and a wire diameter, and then to design a micro spring that satisfies the bounds of (1) and (2). The requirement of the micro spring force ranges for $\theta \in [0, \pi/2]$ can be further formulated in (3) based on (1) and (2):

$$\frac{r_1}{r_2} \hat{F}_w^{A \to M}(\theta) + \frac{\tau_f}{r_2} < F_s(\theta) < \frac{r_1}{r_2} \hat{F}_w^{M \to A}(\theta) - \frac{\tau_f}{r_2}, \tag{3}$$

where F_s denotes the micro spring's pulling force; $\hat{F}_w^{A \to M}$ and $\hat{F}_w^{M \to A}$ represent the effective force of the SMA wire during the material's phase transformations; r_1 and r_2 are the lever arms of $\hat{F}_w$ and F_s respectively. $\hat{F}_w$ can be calculated by

$$\hat{F}_w = 2 \sigma A \cos\left(\frac{\theta}{2}\right), \tag{4}$$

where θ is the wiping blade rotation angle. The lengths of $z - a$ and $z - b$ in Fig. 3(a) are denoted as $L_{za} = L_{zb}$. A is the cross section area of the SMA wire. σ is the SMA wire stress which is governed by the one-dimensional constitutive equation in (5) [21]

$$\sigma = \sigma_0 + D(\xi)(\epsilon - \epsilon_0) - \epsilon_L D(\xi)(\xi - \xi_0) + \Theta(T - T_0), \tag{5}$$

where the subscript "0" indicates an initial state. ϵ and ϵ_L represent the SMA strain and maximum recoverable strain respectively. T is the SMA temperature. Θ is the thermal expansion coefficient which is in a neglectable term due to its small value. $\xi = \xi_S + \xi_T$ is the martensite fraction that consists of stress induced fraction ξ_S and temperature induced fraction ξ_T. $D(\xi)$ is the Young's modulus for the

SMA which can be estimated in (6) during the SMA phase transformation:

$$D(\xi) = D_A + \xi(D_M - D_A), \tag{6}$$

where D_A is the 100% austenite modulus value and D_M is the 100% martensite modulus value.

In order to design a micro spring that satisfies (3), we need to find the lower bound of $\hat{F}_w^{M \to A}$ and the upper bound of $\hat{F}_w^{A \to M}$ which involve determining the SMA wire stress described in (5). Fig. 4(a) demonstrates the relationship between the SMA temperature and the applied stress σ for the material's phase transformation. In phase 1, we set the constant temperature $T = A_f$ to determine the lower bound of $\hat{F}_w^{M \to A}$. Upon the changing of applied stress σ, the SMA presents its pseudo-elastic behavior that is shown in Fig. 4(a) (the red vertical line). When σ is below σ_{cr}^Q, the SMA is in 100% austenite phase with $D(\xi = 0) = D_A$, and it exhibits linear elastic strain

$$\epsilon_Q = \sigma_{cr}^Q / D_A, \tag{7}$$

which occupies a very low proportion of ϵ_L. The SMA phase transformation from austenite to stressed-induced detwinned martensite occurs when the applied stress is in the range of $\sigma_{cr}^Q < \sigma < \sigma_{cr}^{Q'}$ which results in the maximum recoverable strain ϵ_L at $\sigma = \sigma_{cr}^{Q'}$. The stress-strain curve of the above process governed by (5) is illustrated in Fig. 4(b) (the upper curve). σ_{cr}^Q is the lower bound stress for $\hat{F}_w^{M \to A}$ in (3).

Similarly, to determine the upper bound of $\hat{F}_w^{A \to M}$ for (3) in phase 2, we consider the stress change at $T = M_s$ (martensite transformation start) which is approached from A_f. By increasing σ above σ_{cr}^P, the SMA starts transforming from 100% austenite ($D(\xi = 0) = D_A$) to detwinned martensite, as shown in Fig. 4(a) (the blue vertical line). The stress-strain relationship in this process is illustrated in the lower curve of Fig. 4(b). The upper bound stress for $\hat{F}_w^{A \to M}$ shows as $\sigma_{cr}^{P'}$.

Property	Value
Martensite finish temperature M_f (°C)	22.1
Martensite start temperature M_s (°C)	41.4
Austenite start temperature A_s (°C)	50.6
Austenite finish temperature A_f (°C)	68.1
Stress influence coefficient C_M (MPa°C^{-1})	6.05
Stress influence coefficient C_A (MPa°C^{-1})	14.25
Young's modulus at 100%austenite D_A (GPa)	71.7
Young's modulus at 100%martensite D_M (GPa)	12.5
Critical stress σ_{cr}^{P} (MPa)	50.6
Critical stress $\sigma_{cr}^{P'}$ (MPa)	120.3
Maximum recoverable strain ϵ_L	0.045

The critical stresses σ_{cr}^{P} and $\sigma_{cr}^{P'}$ can be considered as constant mechanical properties after the wire cycles sufficient times. σ_{cr}^{Q} can be calculated in (8):

$$\sigma_{cr}^{Q} = \sigma_{cr}^{P} + C_M(T - M_s), \tag{8}$$

where $T = A_f$ and C_M is the stress influence coefficient.

By using $\sigma_{cr}^{P'}$, (8) and (4) to substitute $\hat{F}_w^{M \to A}$ and $\hat{F}_w^{A \to M}$ in (3), we derive the following boundary condition (9) and equations (10), (11) to design a compatible micro spring.

$$F_L < F_s(\theta) < F_U \tag{9}$$

where

$$F_U = \frac{2r_1 A}{r_2} \cos\left(\frac{\theta}{2}\right) \left(\sigma_{cr}^{P} + C_M(A_f - M_s)\right) - \frac{\tau_f}{r_2}, \tag{10}$$

$$F_L = \frac{2r_1 A}{r_2} \cos\left(\frac{\theta}{2}\right) \sigma_{cr}^{P'} + \frac{\tau_f}{r_2}. \tag{11}$$

The extension force of the micro spring is formulated as

$$F_s(\theta) = k\left(r_2\left(\frac{\pi}{2} - \theta\right) + \Delta x\right) + F_i, \tag{12}$$

where k is the spring rate; Δx denotes the spring's length deformation at $\theta = \pi/2$; and F_i is the spring initial tension. Therefore, the design objective of this work can thus be simplified to identify k and F_i of a micro extension spring that satisfy (9).

IV. DESIGN AND PROTOTYPING OF AN EXEMPLARY LENS CLEANING MODULE

In this section, we demonstrate an example design of the lens cleaning module for the *in vivo* robotic camera developed in our prior work [6]. Based on the actuation mechanism design method presented in Section III, a micro extension spring is designed and manufactured. The other major components of the module were also developed for integrating a functional prototype.

A. Lens Cleaning Module Structural Dimensions

Fig. 5 shows the prototype of the lens cleaning module and the major components. The outer diameter of this module is designed as $\phi_1 = 16$ mm to match our robotic camera [6]. The module thickness above the glass cover is $h_1 = 3$ mm. The lengths of lever arms for the wire and the micro spring are $r_1 = 1.2$ mm and $r_2 = 1.64$ mm. The diameter and thickness of the optical glass cover are $\phi_2 = 7$ mm and $h_2 = 1.35$ mm
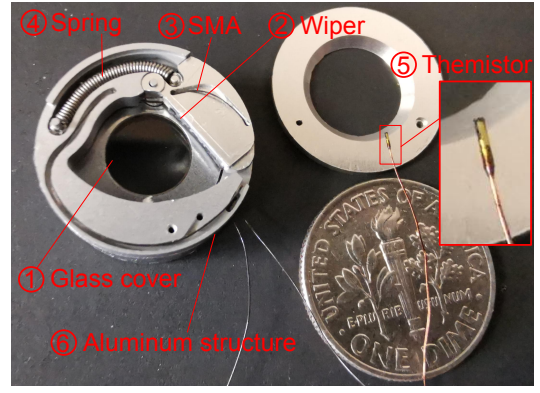

Fig. 5. Prototype design of the lens cleaning module.
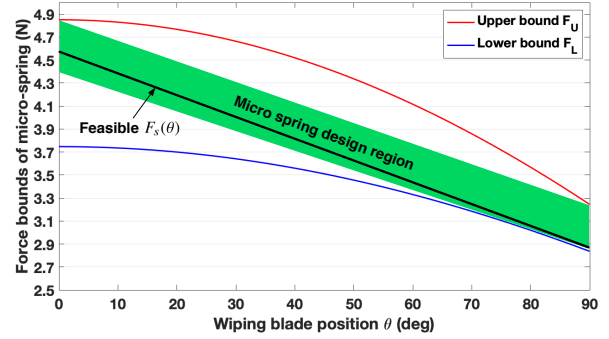

Fig. 6. Computed force bounds for the micro extension spring design. The green area indicates the feasible design region.

respectively. We employed anodized 6061 aluminum alloy with great electrical insulation and mechanical properties, as illustrated in Fig. 5⑥.

B. Optical Glass Cover and Wiping Blade

The effectiveness of the lens cleaning function depends on contact motion between the glass cover and the wiping blade. To guarantee minimum influence on the imaging sharpness, K9 crystal glass, as shown in Fig. 5①, is adopted which has above 99.4% visible light transmittance and great anti-scratch ability. The rubber blade, as shown in Fig. 5②, is manufactured by using ethylene propylene diene monomer (EPDM) rubber compounds with added polytetrafluoroethylene (PTFE) to achieve low contact friction with the glass cover. Our measurements indicate the frictional coefficient μ between the rubber blade and the glass cover is about 0.4.

In order to have good contact between the two parts, we design the rubber blade 0.2 mm thicker than the height clearance, which means the rubber blade is squeezed to fit into the contacting space. According to our experiment, $F_N = 0.49$ N is required to apply on the rubber blade for obtaining the 0.2 mm indention. The frictional torque τ_f in (9), (10) and (11) can be estimated by $\tau_f = \mu F_N r_3 = 1.04$ mN m, where $r_3 = 5.23$ mm is the average lever arm length of the wiping blade.

C. SMA Wire

The selection of an SMA wire, including material type, wire diameter and length, is case-dependent. The material

type determines an SMA's mechanical properties, such as transformation temperatures (M_f, M_s, A_s, A_f), maximum recoverable strain ϵ_L, etc. Based on a specified SMA material, the wire diameter determines the maximum allowable actuation force and affects heat convection rate. The wire length determines the maximum actuation distance during the SMA's phase transformation.

According to the above considerations, we employ an HT Flexinol® Ni-Ti SMA wire with a diameter of 0.15 mm (Dynalloy, Inc.), as illustrated in Fig. 5③. We conducted experiments to measure the SMA material properties, which are presented in Table I. The required wire contraction distance $L_{ab}^{max} = \sqrt{2}r_1$ for enabling the wiping blade rotation with $\theta \in [0, \pi/2]$, as shown in Fig. 3(a), demands the total wire length L

$$L > L_{ab}^{max}/(\epsilon_L - \epsilon_Q). \tag{13}$$

The purpose of introducing ϵ_Q in (13) is to avoid the region of linear elastic strain, as shown in Fig. 4(b). ϵ_Q is calculated as 0.4% by using (7), (8) and the data in Table I. Subsequently, we can determine the requirement for the SMA wire length $L > 36.92$ mm. In this prototype, the wire length is designed as 42 mm.

D. Micro Extension Spring Design

Fig. 6 illustrates the force bounds and feasible region for designing the micro extension spring. In accordance with the determined parameters in this section for (10) and (11), the force bounds $F_U(\theta)$ and $F_L(\theta)$ are specified. The black line in the green region exemplify a feasible spring force-displacement function for (12). In this work, we use $F_s(\theta = 0) = 4.6$ N and $F_s(\theta = \pi/2) = 2.85$ N for designing the micro spring. Considering the dimensional constraints of the spring in this example design, we complete the spring design with the aid of Advance Spring Design software (Universal Technical Systems, Inc.). Fig. 5④ shows the manufactured micro spring with music wire material by Newcomb Spring Corp.

E. SMA Temperature Sensing

To control phase transformation of the SMA wire, real time temperature sensing is needed. In this design, we integrate a micro thermistor (223Fμ3122-07U015, Semitec USA Corp.) in the module to detect the SMA temperature, as shown in Fig. 5⑤.

V. EXPERIMENTS

The experiments aim to evaluate the performance of our proposed lens cleaning module. Actuation cycles were initially investigated.

A. Actuation Cycle

The lens cleaner's actuation cycle is determined by the rate of SMA phase transformation, which is influenced by Joule heating, heat convection, and bias stress. The experiment setup for testing the actuation cycle is illustrated in Fig. 7. We employ a camera with a frame rate of 60 frames per second to record the actuation cycle. The SMA wire is terminated
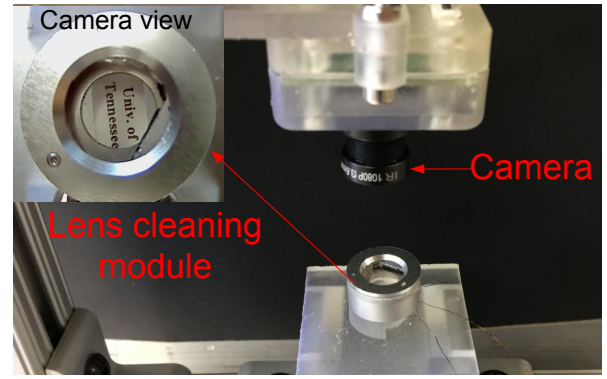

Fig. 7. Experiment setup for evaluating actuation cycle and cleaning efficiency of the lens cleaning module.

TABLE II
REQUIRED TIME FOR HEATING THE SMA FROM $T_0 = 23°$C TO $\tilde{A}_f = 76.6\,°$C

	Current (mA)			
	500	700	900	1100
Time (s)	3.47	2.51	0.95	0.73
Struct. temp. (°C)	59.6	45.8	39.1	33.2

inside the module, and connects to a current source via electrical wires and a MOSFET switch which is controlled by a micro-controller. The thermistor attached on the SMA also connects to the micro-controller for providing temperature feedback.

1) Duration of Phase 1: By Joule heating, the SMA wire starts to execute the phase 1 as illustrated in Fig. 2. The austensite finish temperature $\tilde{A}_f$ is related to the bias stress and the SMA material properties in Table I, and formulated by

$$\tilde{A}_f = \frac{\sigma_m}{C_A} + A_f, \tag{14}$$

where σ_m is the maximum bias stress at the end of phase 1. Based on our design ($\sigma_m = 120.8$ MPa, $C_A = 14.2$ MPa °C^{-1}, A_f=68.1 °C), $\tilde{A}_f$ is calculated as 76.6 °C.

We conduct experiments with constant current inputs that range from 500 mA to 1100 mA for heating the SMA wire to reach $\tilde{A}_f$. In addition, we monitor the temperature change on the aluminum structure by using a thermal camera (Duo Pro R, FLIR Systems Inc.). Table II shows the aluminum structure temperatures and the required time to complete the phase 1 under different current inputs. The results indicate that a smaller current such as 500 mA led to a longer heating period 3.47 s which can elevate the temperature of the aluminum structure to 59.6 °C. In contrast, a higher input current 1100 mA only took 0.73 s to heat the SMA wire to $\tilde{A}_f$. The aluminum structure temperature slightly increased to 33.2 °C.

2) Duration of Phase 2 and Full Cycle: In this test, we demonstrate duration of the phase 2 by consecutively actuating five full cycles. We apply 1000 mA current input during phase 1 for each cycle. The results are demonstrated in Table III. The cooling period increased from 1.29 s to 2.31 s by activating the module 5 times. The full cycle also
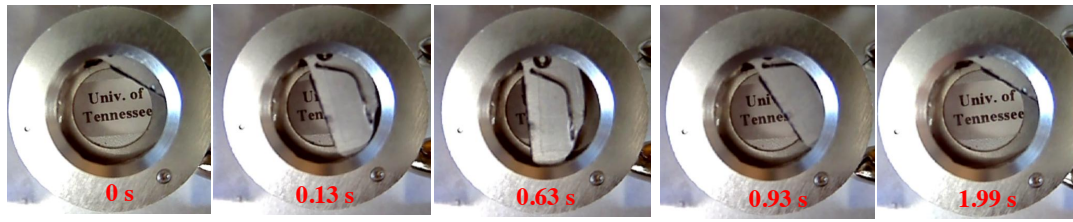
Fig. 8. Demonstration of an actuation cycle. The input current for the heating period is set at 1000 mA.

TABLE III

DURATIONS OF PHASE 2 IN FIVE CONSECUTIVE CYCLES BY USING INPUT CURRENT AT 1000 mA ($T_0 = 23\,°C$)

	Cycle Number				
	1	2	3	4	5
Phase 2 (s)	1.26	1.41	1.63	1.92	2.31
Full cycle (s)	1.99	2.15	2.39	2.65	2.97
Struct. temp. (°C)	34.3	36.5	40.2	46.7	57.2

extended from 1.99 s to 2.97 s. Fig. 8 demonstrate the first full actuation cycle with time stamps.

VI. CONCLUSION

Aiming to address the lens fogging and soiling problems during laparoscopic surgery, we developed an *in vivo in situ* lens cleaning module for laparoscopic cameras. This design is capable of providing surgeons minimal intraoperative visual interruption to clean a contaminated lens, which is especially important for fully insertable robotic cameras. Due to the modularized design, it can be integrated in other robotic camera systems which operate in complex environments such as the human body cavity. The experimental tests indicated that the actuation speed for a single cycle was about 0.5 Hz. In our future work, we plan to integrate the module in our robotic camera for *in vivo* tests. Design improvements such as increasing the actuation frequency to 1 Hz will also be considered by introducing micro-scale forced heat convection system in the lens cleaning module.

REFERENCES

[1] S. Spaner and G. Warnock, "A brief history of endoscopy, laparoscopy, and laparoscopic surgery," *J Laparoendosc Adv Surg Tech A*, vol. 7, no. 6, pp. 369–373, 1997.

[2] P. P. Rao, P. P. Rao, and S. B. S, "Single-incision laparoscopic surgery - current status and controversies," *Journal of Minimal Access Surgery*, vol. 7, no. 1, pp. 6–16, 2011.

[3] M. Simi, M. Silvestri, C. Cavallotti, M. Vatteroni, P. Valdastri, A. Menciassi, and P. Dario, "Magnetically activated stereoscopic vision system for laparoendoscopic single-site surgery," *IEEE/ASME Trans. Mechatronics*, vol. 18, no. 3, pp. 1140–1151, 2013.

[4] X. Liu, G. J. Mancini, Y. Guan, and J. Tan, "Design of a magnetic actuated fully insertable robotic camera system for single-incision laparoscopic surgery," *IEEE/ASME Trans. Mechatronics*, vol. 21, no. 4, pp. 1966–1976, 2016.

[5] C. A. Castro, A. Alqassis, S. Smith, T. Ketterl, Y. Sun, S. Ross, A. Rosemurgy, P. P. Savage, and R. D. Gitlin, "A wireless robot for networked laparoscopy," *IEEE Trans. Biomed. Eng.*, vol. 60, no. 4, pp. 930–936, 2013.

[6] X. Liu, R. Y. Abdolmalaki, T. Zuo, Y. Guan, G. J. Mancini, and J. Tan, "Transformable in-vivo robotic laparoscopic camera with optimized illumination system for single-port access surgery: Initial prototype," *IEEE/ASME Transactions on Mechatronics*, vol. 23, no. 4, pp. 1585–1596, 2018.

[7] X. Liu, R. Y. Abdolmalaki, G. J. Mancini, and J. Tan, "Optical design of an in vivo laparoscopic lighting system," *Journal of Biomedical Optics*, vol. 22, pp. 22 – 22 – 15, 2017.

[8] M. A. Cassera, T. A. Goers, G. O. Spaun, and L. L. Swanström, "Efficacy of using a novel endoscopic lens cleaning device: a prospective randomized controlled trial.," *Surgical innovation*, vol. 18 2, pp. 150–5, 2011.

[9] T. Manning, N. Papa, M. Perera, S. McGrath, D. Christidis, M. Khan, R. O'Beirne, N. Campbell, D. M. Bolton, and N. L. Lawrentschuk, "Laparoscopic lens fogging: solving a common surgical problem in standard and robotic laparoscopes via a scientific model," *Surgical Endoscopy*, vol. 32, pp. 1600–1606, 2017.

[10] N. Yong, P. Grangé, and D. Eldred-Evans, "Impact of laparoscopic lens contamination in operating theaters: A study on the frequency and duration of lens contamination and commonly utilized techniques to maintain clear vision.," *Surgical laparoscopy, endoscopy & percutaneous techniques*, vol. 26 4, pp. 286–9, 2016.

[11] D. Kreeft, E. A. Arkenbout, P. W. J. Henselmans, W. R. van Furth, and P. Breedveld, "Review of techniques to achieve optical surface cleanliness and their potential application to surgical endoscopes," *Surgical Innovation*, vol. 24, no. 5, pp. 509–527, 2017.

[12] E. R. H. Sutton, Y. Youssef, N. Meenaghan, C. Godínez, Y. Xiao, T. H. Lee, D. J. Dexter, and A. Park, "Gaze disruptions experienced by the laparoscopic operating surgeon," *Surgical Endoscopy*, vol. 24, pp. 1240–1244, 2009.

[13] N. L. Lawrentschuk, N. E. Fleshner, and D. M. Bolton, "Laparoscopic lens fogging: a review of etiology and methods to maintain a clear visual field.," *Journal of endourology*, vol. 24 6, pp. 905–13, 2010.

[14] S. Anderson, J. Zimmerman, E. Houston, K. Farino, and N. Begg, "Design of an endoscope lens shielding device for use in laparoscopic procedures," *Journal of Medical Devices*, vol. 4, pp. 027515–027515–1, 08 2010.

[15] E. C. Miller, G. Schmitz, and S. M. Smith, "Endoscopic lens cleaner." US patent 2009/0105543, 2009.

[16] F. Brody and Bethesda, "Minimally invasive lens cleaner." US patent 2016/0022367 A1, 2016.

[17] C. O'Prey, C. A. Clark, and A. I. Fleming, "Endoscope wiper blade cleaner." US patent 9,763,567 B2, 2017.

[18] H. Tatsuki, T. Yokobori, C. Katayama, R. Kato, R. Takahashi, K. Osone, T. Takada, R. Yajima, Y. Motegi, H. Ogawa, T. Fujii, K. Shirabe, H. Kuwano, and T. Asao, "A novel one-step lens cleaning device using air and water flow for endoscopic surgery," *PLOS ONE*, vol. 13, pp. 1–9, 07 2018.

[19] A. R. Yazdanpanah, X. Liu, N. Li, and J. Tan, "A novel laparoscopic camera robot with in-vivo lens cleaning and debris prevention modules," in *2017 IEEE/RSJ International Conference on Intelligent Robots and Systems (IROS)*, pp. 3669–3674, Sept 2017.

[20] K. Tanaka, S. Kobayashi, and Y. Sato, "Thermomechanics of transformation pseudoelasticity and shape memory effect in alloys," *International Journal of Plasticity*, vol. 2, no. 1, pp. 59 – 72, 1986.

[21] L. Brinson, "One-dimensional constitutive behavior of shape memory alloys: Thermomechanical derivation with non-constant material functions and redefined martensite internal variable," *Journal of Intelligent Material Systems and Structures*, vol. 4, no. 2, pp. 229–242, 1993.